Chinese Chemical Letters 37 (2026) 111038

Contents lists available at ScienceDirect

Chinese Chemical Letters

journal homepage: www.elsevier.com/locate/cclet

Solvothermal domino synthesis of an ER-targeted iron(II) complex for inducing immunogenic cell death

Ning Tian[a,1], Haoyu Ju[b,1], Qian Hu[b], Qifeng Hou[a], Yiping Lu[b], Yu Liu[a], Jinmei Huang[a], Zhong-Hong Zhu[a], Bin Zhang[a], Jin Huang[b,*], Ming-Hua Zeng[a,c,*]

[a] School of Chemistry and Pharmaceutical Sciences, State Key Laboratory for Chemistry and Molecular Engineering of Medicinal Resources, Guangxi Normal University, Guilin 541004, China
[b] Shanghai Frontiers Science Center of Optogenetic Techniques for Cell Metabolism, Shanghai Key Laboratory of New Drug Design, School of Pharmacy, East China University of Science and Technology, Shanghai 200237, China
[c] College of Chemistry and Bioengineering, Guilin University of Technology, Guilin 541004, China

ARTICLE INFO

Article history:
Received 3 January 2025
Revised 18 February 2025
Accepted 5 March 2025
Available online 5 March 2025

Keywords:
Domino reaction
Metal complex
Antitumor
Endoplasmic reticulum targeted
Immunogenic cell death

ABSTRACT

Reactive oxygen species (ROS)-based endoplasmic reticulum (ER) stress is a prerequisite for the induction of immunogenic cell death (ICD), and the development of metal-based ICD inducers has garnered significant attention. However, the drug-target mechanisms of ICD inducers still require further exploration. Herein, we reported an ER-targeting iron(II) complex (Fe-NBM) as an ICD inducer, which was obtained through a solvothermal domino reaction. Accordingly, pyridin-2-ylmethanamine and 1-methyl-2-formylbenzimidazole underwent consecutive covalent transformations to form a novel *N*-heterocyclic ligand, which subsequently coordinated with ferrous chloride to directly yield the crystalline Fe-NBM in one pot. Confocal laser scanning microscope (CLSM), molecular docking and cellular thermal shift assay (CETSA) showed that Fe-NBM could specifically target the ER by binding to the IRE1α (Inositol requiring kinase enzyme 1 alpha) and induce ICD by generating ROS-based ER stress. In an immunocompetent mouse model, Fe-NBM could significantly inhibit tumor growth and stimulate anti-tumor immunity, and exhibit an enhanced effect when combined with anti-PD1 therapy, leading to near-complete tumor elimination. To gain deeper understanding of how to synthesize such effective ICD inducers at the molecular level, a combination of electrospray ionization mass spectrometry (ESI-MS) and crystallography was employed for thoroughly tracking the step-economy synthetic process. To the best of our knowledge, Fe-NBM is the first iron-based ICD inducer that directly targets ER through binding to IRE1α. We believe that the ICD-related target information presented in this work will enhance our understanding of the molecular mechanisms underlying ICD and facilitate the design of new ICD inducers.

© 2026 Published by Elsevier B.V. on behalf of Chinese Chemical Society and Institute of Materia Medica, Chinese Academy of Medical Sciences.

Immunogenic cell death (ICD) has emerged as a promising approach in cancer immunotherapy, capable of eliciting an adaptive immune response for long-lasting inhibition of tumor metastasis and recurrence [1,2]. Endoplasmic reticulum (ER) stress and reactive oxygen species (ROS) production are considered as essential components of the intracellular pathways that induce ICD [3]. More importantly, ER-targeted ICD inducers can induce a stronger ROS-based ER stress, which is more efficient in activating the tumor immunogenicity [4].

Continuous efforts have been devoted towards novel ICD inducers that can effectively trigger ER stress, and in recent years, a significant increase in the number of small molecules has been documented as potential ICD inducers [5]. Specially, accumulated attention is emphasized on the metal complexes [6], due to their appealing biological properties [7], distinctive catalytic properties [8], highly editable ligands and specific subcellular organelle localization [9], which may enhance ROS-based ER stress. A series of anticancer metal complexes based on platinum [10–15], iridium [16–21], ruthenium [22–24], gold [25–28] and copper (Table S1 in Supporting information) [29–31], have been identified to induce an immune response against tumor cells by triggering ICD. However, as far as we know, only a few of them can selectively target the ER for effective immune responsiveness (Fig. S1 in Supporting information). Meanwhile, the specific biotarget of these reported ICD

* Corresponding authors.
E-mail addresses: huangjin@ecust.edu.cn (J. Huang), zmh@mailbox.gxnu.edu.cn (M.-H. Zeng).
[1] These authors contributed equally to this work.

https://doi.org/10.1016/j.cclet.2025.111038
1001-8417/© 2026 Published by Elsevier B.V. on behalf of Chinese Chemical Society and Institute of Materia Medica, Chinese Academy of Medical Sciences.

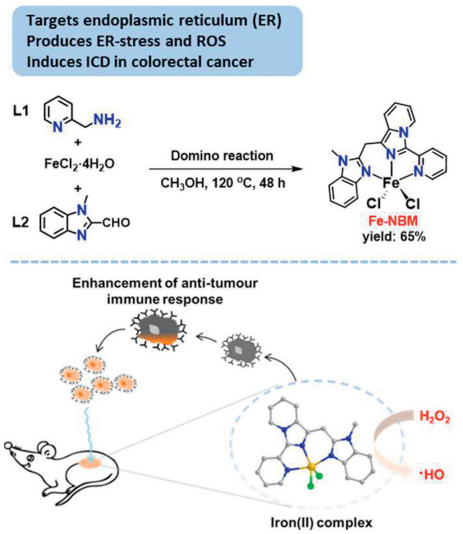
inducers is still not very clear (Table S2 in Supporting information) [17]. Therefore, elucidating the action mode of ICD at the molecular target level is very urgent, and is helpful for the rational design of new inducers with improved efficacy.

On the other hand, due to the pivotal role of heterocycles and their metal complexes played in cancer immunotherapy [5,32], the development of novel synthetic methodologies for constructing metal complexes with innovative heterocyclic frameworks offers new approaches for the discovery of anticancer agents with unique mechanisms of action [6]. We have recently developed a series of solvothermal domino reactions for directly synthesizing well-configured metal complexes from simple heteroaromatic ring-containing substrates and metal salts in one pot [33–35]. Several bioimaging and anti-tumor novel agents have been synthesized through this step-economy strategy [36,37]. We believe that this approach may also provide a platform for accessing potential metal-based ICD inducers.

In this study, the iron(II) complex, Fe-NBM, containing an *in-situ* formed *N*-heterocyclic ligand, was synthesized *via* a solvothermal domino reaction from pyridin-2-ylmethanamine (**L1**), 1-methyl-2-formylbenzimidazole (**L2**) with ferrous chloride in one pot. When the reaction was finished, crystalline Fe-NBM was directly obtained by filtering the reaction solution without further isolation or purification. Besides, the reaction mechanism was disclosed by electrospray ionization mass spectrometry (ESI-MS) and crystallography. Through confocal laser scanning microscope (CLSM), molecular docking and cellular thermal shift assay (CETSA), we found that Fe-NBM targeted the ER by binding to Inositol requiring kinase enzyme 1 alpha (IRE1α) [38], a highly conserved transmembrane protein which locates at the ER and triggered ROS-based ER stress ultimately leading to the progression of ICD. Moreover, cell-based and *in vivo* experiments indicated that Fe-NBM could induce ICD and enhanced the effect of anti-PD1 immunotherapy. In all, we present here the first iron-based complex as an ICD inducer which targets the ER through binding to IRE1α, promising for designing metal-based ICD with better performance.

Pyridin-2-ylmethanamine (**L1**, 0.5 mmol), 1-methyl-2-formylbenzimidazole (**L2**, 0.5 mmol) and $FeCl_2{\cdot}4H_2O$ (1.0 mmol) were dissolved in MeOH (10 mL) at room temperature. Subsequently, the reaction mixture was stirred for 10 min and transferred to a teflon-lined steel bomb and subjected to oven heating at 120 °C for 48 h. The dark red crystals {1-methyl-2-((3-(pyridin-2-yl)imidazo[1,5-*a*]pyridin-1-yl)methyl)-1*H*-benzo[*d*]imidaz-ole}$FeCl_2$ (Fe-NBM) were obtained simply by filtering the cooled reaction solution, yield: 65 %, based on **L1** (Scheme 1, Figs. S2 and S3 in Supporting information). This synergistic organic-inorganic synthesis markedly enhances the efficiency of the construction of similar complexes.

Fe-NBM ($[Fe^{II}(C_{21}H_{17}N_5)Cl_2]$) crystallizes in the monoclinic space group $P2_1/c$ (Table S3) and the asymmetric unit consists of one iron ion, two chloride ions, and the *in-situ* formed ligand **L6** (**L6** = (1-methyl-2-((3-(pyridin-2-yl)imidazo[1,5-*a*]pyridin-1-yl)methyl)-1*H*-benzo[*d*]imidazole). The organic ligand **L6** was extracted from Fe-NBM and identified by NMR and ESI-MS (Fig. S4 in Supporting information). The +2 valence of the iron ion in Fe-NBM was confirmed by ^{57}Fe Mössbauer spectra (Fig. S5 in Supporting information). By *SHAPE* analyzing, the Fe^{2+} was determined to five-coordinated with a trigonal bipyramid geometry (Table S4 in Supporting information). The bond length of Fe-Cl lies in 2.336-2.340 Å, and the angle of Cl-Fe-Cl is 109.47° (Table S5 in Supporting information). Intramolecular non-covalent interactions were presented in Fig. S6 and Table S6 (Supporting information). ESI-MS of Fe-NBM dissolved in CH_3OH and H_2O indicates the molecular entity is stable with seven different fragments containing the [Fe^{II}(**L6**)] moiety observed, where [Fe^{II}(**L6**)$(H_2O)]^{2+}$ (m/z = 206.5461), $[Fe^{II}(\mathbf{L6})_2]^{2+}$ (m/z = 367.1147), and [Fe^{II}(**L6**)Cl]$^+$

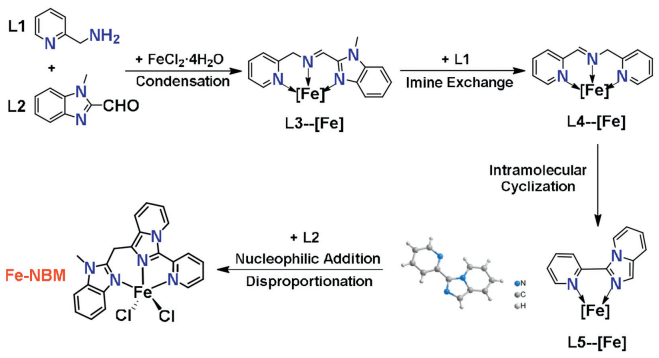


Scheme 1. Synthetic routine of Fe-NBM and schematic presentation of the immunotherapy by Fe-NBM.

(m/z = 430.0508) are the dominant species (Figs. S7 and S8, Table S7 in Supporting information). PXRD, TG, IR, and elemental analyses (Figs. S9-S11 in Supporting information) confirmed the phase purity of the bulk product. Elemental analyses calcd. (%) for $Fe(C_{21}H_{17}N_5)Cl_2$ (Fe-NBM): C 53.91, H 3.61, N 15.82. Found: C 54.11, H 3.68, N 15.02. IR data for Fe-NBM (KBr, cm^{-1}): 3427.17 (s), 1596.21 (w), 1488.99 (s), 1461.41 (m), 1419.10 (w), 1310.61 (w), 1251.94 (m), 1147.02 (w), 1080.69 (w), 1013.38 (w), 779.19 (m), 745.82 (s), 681.75 (m). The stability test using UV-vis spectra and HPLC demonstrated that Fe-NBM was stable in phosphate buffer saline (PBS) for up to 48 h (Figs. S12 and S13 in Supporting information).

A possible mechanism for the synthesis of Fe-NBM was illustrated in Scheme 2 and Fig. S16 (Supporting information). Key steps of the proposed mechanism involve: aldehyde-amine condensation of **L1** and **L2** to give the imine intermediate (**L3**), imine exchange of **L3** to provide 1,3-dipyridyl-imine (**L4**), intramolecular cyclization of **L4** to give imidazo[1,5-*a*]pyridine (**L5**), nucleophilic addition of **L5** with **L2** followed by disproportionation reaction to afford Fe-NBM. To provide support for the above mechanism, the domino reaction was monitored by time-dependent ESI-MS, both at room temperature and under solvothermal conditions (Fig. S14 in Supporting information).

Firstly, at room temperature, the major organic ions observed corresponded to **L1** ([**L1** + H]$^+$, m/z = 109.0760) and **L2** ([**L2** + H]$^+$, m/z = 161.0706). Moreover, aldehyde-amine condensa-



Scheme 2. Proposed mechanism for the solvothermal domino reaction.

tion products **L3** and **L3'** readily coordinated with Fe^{II} to form corresponding coordinative ions $[Fe^{II}(\mathbf{L3})_2]^{2+}$ or $[Fe^{II}(\mathbf{L3'})_2]^{2+}$ at $m/z = 278.0878$, $[Fe^{II}(\mathbf{L3})Cl]^+$ and $[Fe^{II}(\mathbf{L3'})Cl]^+$ at $m/z = 341.0241$. Furthermore, the imine exchange reaction [39] between **L3'** and **L1** yielded 1,3-dipyridyl-imine (**L4**) and its complex $[Fe^{II}(\mathbf{L4})Cl]^+$ and $[Fe^{II}(\mathbf{L4})_2Cl]^+$ at $m/z = 287.9974$, 485.0923. Besides, the byproduct of the imine exchange reaction, (1-methyl-1*H*-benzo[*d*]imidazol-2-yl)methanamine (**L2'**) was also detected at $m/z = 162.1021$. It is noteworthy that at room temperature, neither imidazo[1,5-*a*]pyridine (**L5**) nor Fe-NBM was detected by ESI-MS in the reaction solution, which implies that the reaction can only proceed to **L4** at room temperature (Figs. S14a, S15 and16, Table S8 in Supporting information).

Next, the reaction of **L1**, **L2** and $FeCl_2{\cdot}4H_2O$ was carried out at 120 °C for 0.5-48 h and monitored by ESI-MS (Figs. S14b-g, S15 and 16, Table S8). In addition to the imine intermediates (**L3**, **L3'** and **L4**), **L5** were also detected at $m/z = 285.9818$, corresponding to $[Fe^{II}(\mathbf{L5})Cl]^+$. The intramolecular cyclization from **L4** to **L5** included nucleophilic addition of N atom on pyridine ring to the C=N bond and subsequently aromatization. Five fragments Int-A ($m/z = 485.0923$), Int-A' ($m/z = 538.1191$), Int-C ($m/z = 449.1149$), Int-C' ($m/z = 502.1421$) and Int-D ($m/z = 483.0771$) were simultaneously observed, corresponding to the intramolecular cyclization. Finally, **L5** was observed to react with **L2** *via* nucleophilic addition to produce diary-carbinol (Int-F, $m/z = 446.0448$), which underwent disproportionation to give Fe-NBM ($m/z = 430.0504$) and the byproduct diaryketone (Fe-NBM-O, $m/z = 444.0294$) [34]. To our delight, **L5** was isolated with a shorten reaction time of 3 h, and its structure was confirmed by crystallography, NMR and ESI-MS (Figs. S3 and S17, Table S3 in Supporting information). Furthermore, the isolated **L5** could also react with **L2** to yield Fe-NBM at 120 °C for 48 h. These results clearly confirmed that **L5** was a key intermediate to support the proposed mechanism.

Using 1,3-diphenylisobenzofuran (DPBF) as the indicator for ROS, a significant reduced ultraviolet absorption of DPBF at 410 nm is observed after treated with Fe-NBM and under varying concentrations of H_2O_2 for 30 min (Figs. 1a and b), which indicated that Fe-NBM could facilitate the generation of ROS from H_2O_2. To further confirm the species of the generated ROS, electron spin resonance (ESR) measurement was conducted using 5,5-dimethylpyrroline-*N*-oxide (DMPO) as the spin trap agent. A typical four-line resonance with an intensity ratio of 1:2:2:1 was observed in Fig. 1c, which was assigned to the characteristic signal of the DMPO-·OH adduct [40]. The ESR control experiments, conducted with simple iron salts ($FeCl_2{\cdot}4H_2O$) and the isolated ligand **L6** of Fe-NBM were showed in Fig. S18 (Supporting information). These results indicated that Fe^{2+} endowed Fe-NBM the ability to facilitate the decomposition of H_2O_2 to ·OH. Moreover, cyclic voltammetry (CV) measurement revealed that Fe-NBM exhibited a single anodic peak at the potential of 1.14 V *vs.* Ag/AgCl (Fig. 1d), inferring that Fe-NBM converted H_2O_2 to ·OH by transferring single electron from Fe^{2+} to H_2O_2 (Eq. 1).

$$Fe^{II}\text{–NBM} + H_2O_2 \xrightarrow{H^+} Fe^{III}\text{–NBM} + \cdot OH + H_2O \quad (1)$$

Due to the ability of Fe-NBM to convert H_2O_2 to ·OH in extracellular, we then used DCFH-DA, an active oxygen-specific probe, to detect whether Fe-NBM could also facilitate the generation of intracellular ROS. Fig. 1e indicated that Fe-NBM could enhance the generation of ROS in cells in a dose-dependent manner. Interestingly, in the same conditions, **L6** and $FeCl_2{\cdot}4H_2O$ induced less ROS than Fe-NBM, which suggested that the coordination between Fe^{2+} and **L6** enhanced the ability to induce ROS in intracellular significantly (Fig. S19 in Supporting information). Various ROS scavengers (D-mannitol: ·OH; Tiron: super oxide anion ($\cdot O^{2-}$); ebselen: lipid peroxidation) were then used to determine the species of intracellular ROS induced by Fe-NBM. Among these ROS scavengers, D-mannitol could significantly mitigate the impact of Fe-NBM on cell viability (Fig. S20 in Supporting information), which implied that Fe-NBM treatment could induce the ROS formation in intracellular, and the primary specie was ·OH.

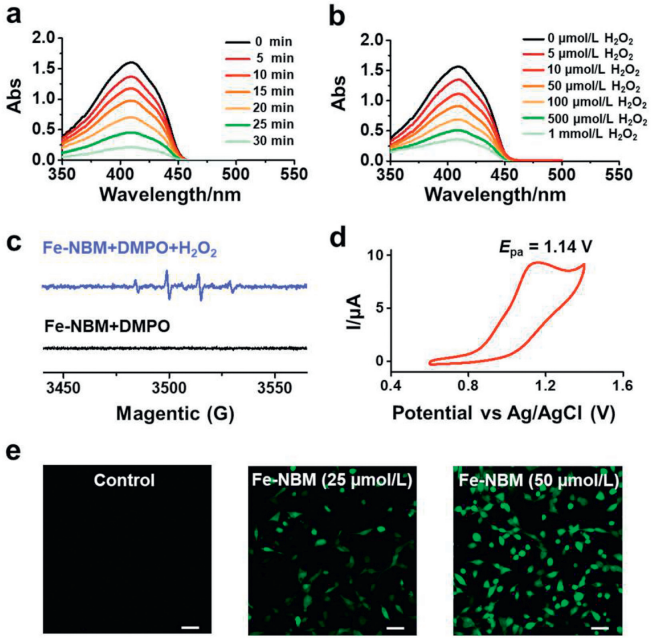


Fig. 1. (a) Time-dependent absorption spectra of DPBF (40 μmol/L) with 5 μmol/L Fe-NBM in the presence of 100 μmol/L H_2O_2. (b) DPBF absorption spectra with 5 μmol/L Fe-NBM under different level of H_2O_2 for 30 min. (c) The ESR spectra of ·OH generated by decomposition of H_2O_2 promoted by Fe-NBM, using DMPO as the ·OH trap. Fe-NBM: 10 μmol/L; H_2O_2: 10 mmol/L. (d) Cyclic voltammetry curve for Fe-NBM (0.5 mmol/L) at room temperature, obtained at the scan rate of 50 mV/s in tetrabutylammonium hexafluorophosphate ($TBA^+PF_6^-$) (0.1 mol/L) electrolyte dissolved in DMF. (e) Confocal laser scanning microscopy images of intracellular ROS in cells treated by Fe-NBM for 24 h and then incubated with DCFH-DA (10 μmol/L) for 1 h. $\lambda_{ex}/\lambda_{em} = 488/525$ nm. Scale bars: 50 μm.

Excessive ROS, especially highly toxic ·OH capable of killing cancer cells, show huge potential in tumor therapy. Numerous ROS-inducing agents have been developed with the aim of inhibiting tumor growth and overcoming therapeutic resistance [41,42]. Since Fe-NBM had the ability to convert H_2O_2 into ·OH both in extracellular and intracellular environment, we examined the cytostatic activity of Fe-NBM. The 3-(4,5-dimethylthiazol-2-yl)-2,5-diphenyltetrazolium bromide (MTT) assay was used to measure the cytotoxic activities of Fe-NBM towards CT26, MDA-MB-231, HeLa, A549 and MCF-7 cancer cells (Fig. 2a). Fe-NBM displayed a high cytotoxic activity towards the CT26 cells, with the half inhibitory concentrations (IC_{50}) value of 8.92 μmol/L while **L6** ($IC_{50} = 58.35$ μmol/L) was less effective than Fe-NBM. Besides, $FeCl_2{\cdot}4H_2O$ was demonstrated with no significant cytotoxic activities, which suggested that the coordination between Fe^{2+} and **L6** led to the better antitumor activity of Fe-NBM (Fig. 2b).

In addition, CT26 cells rounded up and shrunk in size after treated by Fe-NBM (Fig. 2c). The typical morphologies of cell death intuitively showed the anti-tumor activity of Fe-NBM. Flow cytometry analysis with Annexin V/PI double staining also showed an increased population in the AV^+PI^- and AV^+PI^+ in a dose-dependent manner after the Fe-NBM treatment, which presented the cell apoptosis induced by Fe-NBM (Fig. 2d). MTT assay, morphologies of cells and Annexin V/PI co-staining assay demonstrated that Fe-NBM had a significant cytotoxicity.

ROS participates in the progress of protein folding and causes the accumulation of misfolded proteins, which subsequently induces the ER stress, and finally leads to apoptosis [43,44].

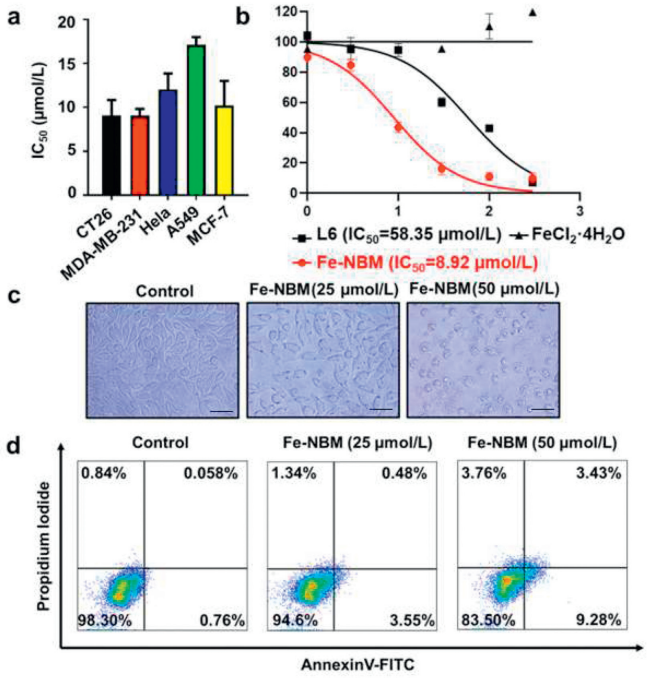


Fig. 2. (a) IC_{50} values of Fe-NBM in different cancer cells. Mean ± S.D. Cells were treated with Fe-NBM for 48 h and incubated with MTT reagent (0.5 mg/mL) for 4 h, then detected the absorbance of the samples at 570 nm. (b) Dose-response curves of cell viability in CT26 cells treated by Fe-NBM, **L6** and $FeCl_2{\cdot}4H_2O$ respectively in CT26 cells. (c) Morphologies of CT26 cells treated with different concentration of Fe-NBM (25 μmol/L, 50 μmol/L), scale bars: 50 μm. (d) Apoptosis analysis of CT26 cell death with the treatment of Fe-NBM. CT26 cells were treated by Fe-NBM for 24 h, then the cells were stained with Annexin V-FITC apoptosis staining/detection kit according to its instructions and analyzed by flow cytometry.

BIP/GRP78 binds to misfolded proteins and prevents them aggregating and triggering ER stress; CHOP is primarily involved in the regulation of apoptosis; Phospho-eIF2α inhibits protein synthesis and reduces the burden on the endoplasmic reticulum. Inspired by the ability of Fe-NBM to generate ROS, we further examined the expression of BIP/GRP78, CHOP, and Phospho-eIF2α [45,46]. According to Figs. 3a and b, we found that compared with the untreated group, Fe-NBM treatment upregulated the expression of BIP/GRP78, CHOP and Phospho-eIF2α, which implied that Fe-NBM could induce ER stress in CT26 cells. Transmission electron microscopy revealed the induction of ER stress in CT26 cells treated with Fe-NBM, characterized by the swelling of the endoplasmic reticulum lumen (Fig. 3c). To clarify if the ER stress was indeed ROS-mediated, we used *N*-acetylcysteine (NAC), a ROS quencher, to pretreat CT26 cells. NAC effectively quenched Fe-NBM induced ROS generation, partially reversed the upregulation of Phospho-eIF2α, and restored the morphology of the endoplasmic reticulum. (Figs. 3d-f). These results suggested that Fe-NBM could induce ROS-based ER stress, which was a critical factor in the signaling cascades leading to ICD.

ER stress is crucial for triggering danger signals and facilitating the trafficking of damage-associated molecular patterns (DAMPs) to stimulate anti-cancer immune responses [3,47]. Additionally, ROS-based ER stress can promote more effective ICD-associated immunogenicity through the enhancement of emission and trafficking of DAMPs [48]. Since our previous results showed that Fe-NBM could induce the ROS-based ER stress, the biochemical hallmarks of ICD, such as ATP, high-mobility group box 1 protein (HMGB1) and calreticulin (CRT) were detected to investigate whether Fe-NBM could also induce ICD [49,50]. Secretion of ATP is important in the progress of ICD, and we found that, compared with the untreated group, the extracellular ATP release was significantly increased and exhibited a dose-dependent increase in Fe-NBM treated cells (Fig. 4a). The release of HMGB1, which is a danger signal during ICD [51,52], was also observed (Fig. 4b). Additionally, we detected the exposed CRT and found that with the increase of Fe-NBM concentration, the fluorescent signal of exposed CRT significantly increased, suggesting that Fe-NBM could induce CRT exposure in CT26 cells (Fig. 4c). Moreover, NAC reversed the ICD-related characteristics caused by Fe-NBM, which further indicated that Fe-NBM induced ICD through ROS-based ER stress (Figs. 4d-f).

To further investigate the impact of Fe-NBM on immune-related genes expression, RNA sequencing (RNA-seq) was performed on CT26 cells with or without Fe-NBM treated. A total of 52,966 genes were identified in RNA-seq analysis. The hierarchical clustering analysis was taken to observe the up and down-regulation genes between samples with or without the treatment of Fe-NBM. There were 2317 significantly differentially expressed genes (|Fold change| $\geq$ 2; p-adjust $<$ 0.05) between control group (without Fe-NBM treated) and Fe-NBM treated group, which 1264 were up-regulated and 1053 were down-regulated (Fig. 4g and Fig. S21a in Supporting information).

Gene otology (GO) annotations described a significant regulation of defensive response and several biological processes after Fe-NBM treated (Fig. S21b in Supporting information). Further GO enrichment analysis of immune system process involved genes indicated that there were significant differences in leukocyte mediated cytotoxicity, killing of cells of other organism and

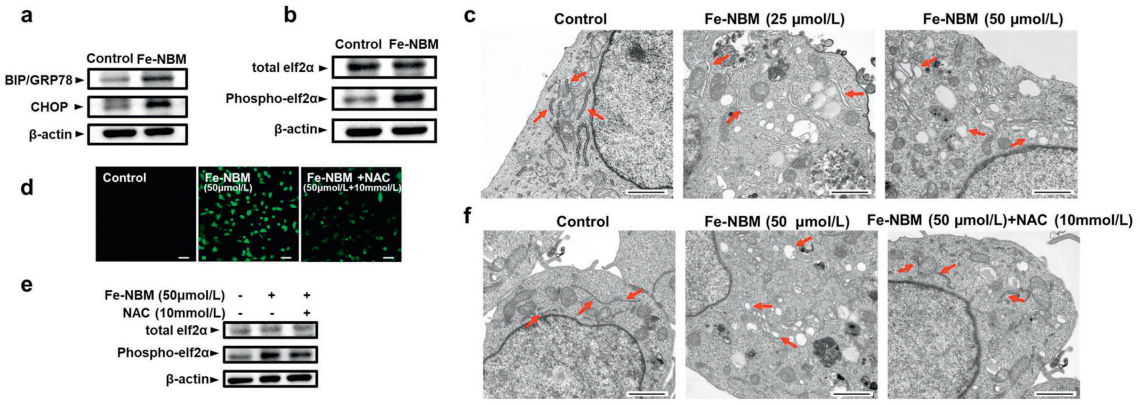


Fig. 3. ER stress induced by Fe-NBM in CT26 cells. (a, b) Western blot assay of BIP/GRP78, CHOP and Phospho-eIf2α in CT26 cells after treated by Fe-NBM for 24 h. (c) ER morphology of CT26 cells treated by Fe-NBM was observed through transmission electron microscopy, scale bars: 1 μm. (d) NAC (10 mmol/L) eliminated the ROS generated by Fe-NBM, scale bars: 50 μm. (e) NAC partially reversed the upregulation of Phospho-eIF2α. (f) NAC restored the morphology of the ER, scale bars: 1 μm.

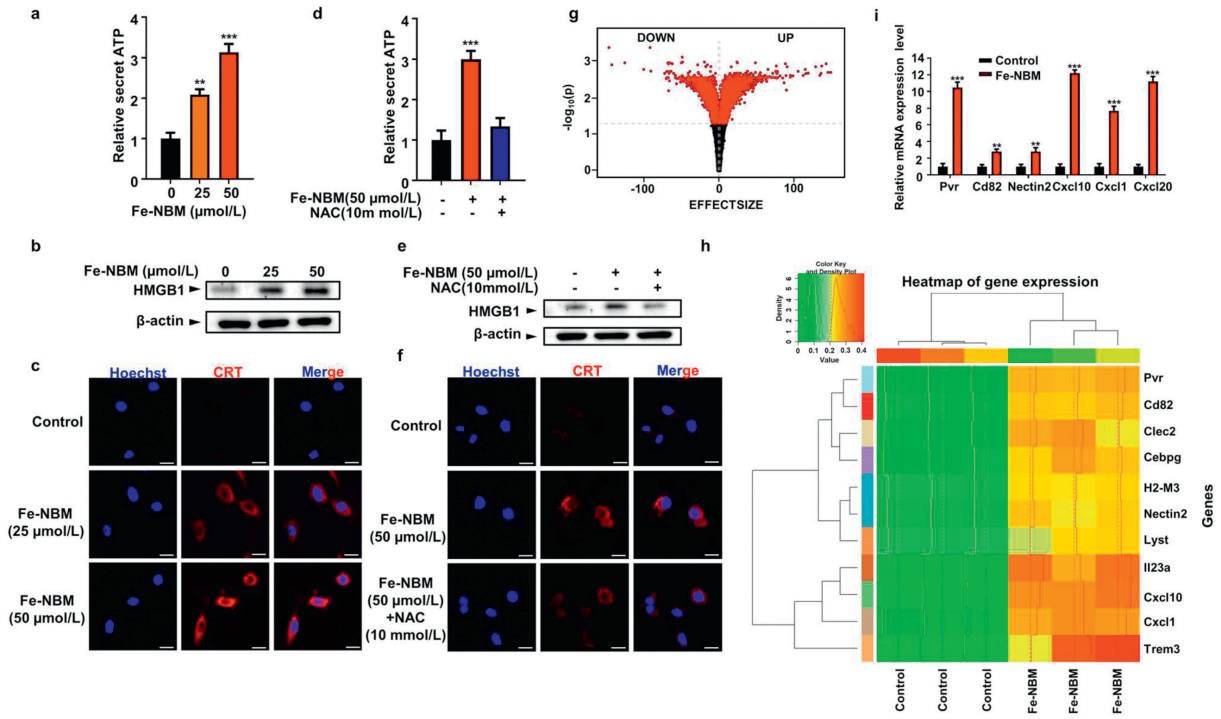


Fig. 4. Fe-NBM can induce ICD associated DAMPs and cause the immune response in CT26 cells. (a) Analysis of secretion of ATP in CT26 cells treated by Fe-NBM. CT26 cells were incubated with Fe-NBM at 37 °C for 12 h and then detected ATP release by ATP Bioluminescent Assay Kit. (b) Western blotting analysis of concentrated conditioned media after treatment of Fe-NBM. (c) The exposure of CRT was imaged through immunostaining of CT26 cells. Scale bars: 20 μm. (d-f) NAC reversed the ICD-related characteristics caused by Fe-NBM. Scale bars: 20 μm. (g) The volcano map of differentially expressed genes with Fe-NBM treatment. (h) Heatmap of significantly up-regulated immune-related gene treated with Fe-NBM in CT26 cells. Each row in the cluster heat map represents one gene and each column represents a sample group. Colours represent the degree of differential gene expression, green to yellow to red means increasing levels of gene expression. (i) qRT-PCR analysis of immune system related genes under the treatment of Fe-NBM in CT26 cells. Mean ± S.D. $^{*}P < 0.05$; $^{**}P < 0.01$; $^{***}P < 0.001$.

complement-dependent cytotoxicity (Fig. S21c in Supporting information). Meanwhile, we observed pronounced increases in the expression of immune-related gene such as Pvr, Cd82, Clec2d, Cebpg, H2-M3, Nectin2, Lyst, Il23a, Cxcl10, Cxcl1, and Trem3 (Fig. 4h). The quantitative reverse transcription polymerase chain reaction (qRT-PCR) analysis further identified the over expression of Pvr, Cd82, Nectin2, Cxcl10, Cxcl1, Cxcl20 (Fig. 4i). The qRT-PCR results were consistent with RNA-seq results, which implied the Fe-NBM could indeed activate the immune response in CT26 cells.

The subcellular localization of Fe-NBM were then investigated through a confocal laser scanning microscope, since that the ligand (**L6**) of Fe-NBM contains an imidazo[1,5-*a*]pyridine moity and displays photophysical properties suitable for bioimaging (Fig. S22 in Supporting information) [53]. The colocalization assay was implemented with Lyso-Tracker Red (LTR), Mito-Tracker Red (MTR) and ER-Tracker Red (ERTR) probe in CT26 cells. As the images showed in Fig. 5a, the signal of Fe-NBM colocalized with ER-Tracker Red with Pearson correlation coefficient of 0.88, calculated by Fiji software. However, the co-staining patterns of Fe-NBM matched poorly with those of LTR and MTR, which indicates that Fe-NBM selectively localized on the ER. To further investigate the mechanism for the ER localization of Fe-NBM, Autodock vina [54] was employed to perform molecular docking of Fe-NBM with the ER localized proteins. Interestingly, during the molecular docking process, the binding affinity between IRE1α and Fe-NBM was superior to other ER localized proteins (Fig. S23 and Table S9 in Supporting information). The 3D structure of IRE1α (PDB ID: 4PL3) was retrieved from the RCSB Protein Data Bank and the binding model of Fe-NBM and IRE1α were presented in Fig. 5b. Fe-NBM was located into a pocket surrounded by Gly-580, Ala-581, Phe-606, Asp-688, Lys-690, His-692, Asn-693, Asp-711, Leu-714, Lys-716, Gly-733 and Thr-734. Moreover, Lys-690 and Lys-716 formed pi-cation interactions with Fe-NBM. CETSA is a novel, label-free, easy and fast strategy for the direct determination of drug binding in intact cells, tissues or lysates, which relies on the thermal stabilization of the protein upon ligand binding [55]. The combination of Fe-NBM and IRE1α was further validated through CETSA approach. As depicted in Figs. 5c and d, the thermal stability of the IRE1α protein increased obviously after treatment with Fe-NBM in a dose-dependent manner. Our results suggested that Fe-NBM acted directly on the ER *via* binding to IRE1α.

Our results suggested that Fe-NBM acted directly on the ER *via* binding to IRE1α. Since IRE1α is a master regulator of the unfolded protein response (UPR), we subsequently evaluated the generation of XBP1s, a spliced form that serves as a stable and functional transcription factor which is produced after IRE1α being activated [56]. We found that after treated with Fe-NBM, CT26 cells showed obvious down-regulation of XBP1s, which indicated the activation of IRE1α might be inhibited through binding with Fe-NBM (Fig. 5e). Moreover, PERK and ATF6 pathway are also important in UPR [57,58]. Fig. 3b showed that phospho-eIF2α, a downstream signal of PERK, were up-regulated after treated by Fe-NBM and Fig. 5f indicated the up-regulation of ATF6, which suggested that Fe-NBM could trigger UPR. The results above indicated that Fe-NBM was able to provoke UPR, which may act with ROS generation, inducing ER stress and enhancing ICD more effectively.

Vaccination assay with immunocompetent, syngeneic mice was a well-established approach to validate ICD *in vivo*. Female BALB/c mice were used to establish an immunocompetent mouse model. The mice of Fe-NBM group were injected with the dying CT26 cells treated by Fe-NBM, while the vehicle group were injected with untreated CT26 cells. One week later, all mice were rechallenged by live CT26 cells (Fig. 6a). All mice in vehicle group were observed the tumor growth by day 15 after rechallenging, whereas no sig-

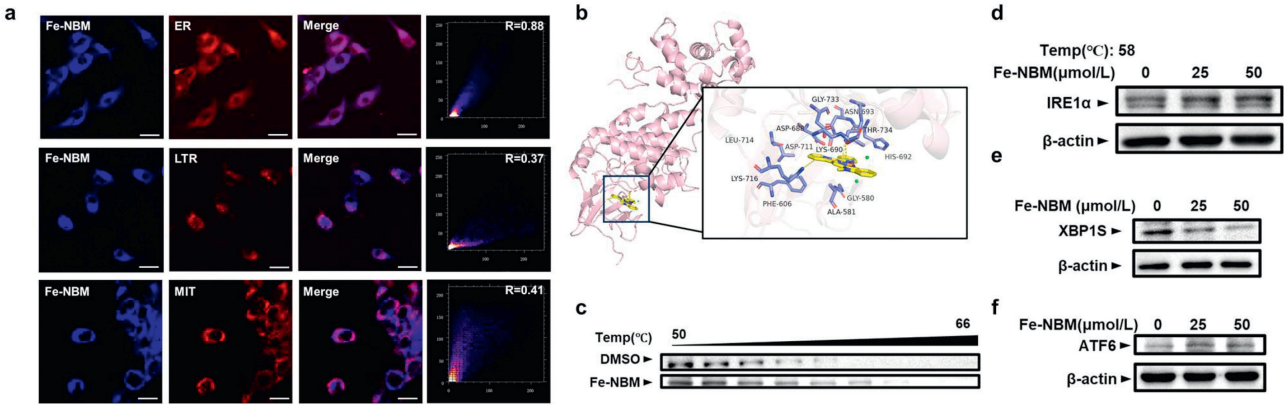


Fig. 5. The subcellular localization of Fe-NBM. (a) Confocal laser scanning microscopy images of CT26 cells upon incubation with Fe-NBM for 4 h and ER-Tracker Red for 0.5 h. The Pearson correlation coefficient was calculated by Fiji software. Scale bars: 20 μm. (b) The 3D binding model of Fe-NBM with the IRE1α protein obtained through molecular docking experiments. (c) Western blot image of CETSA of IRE1α under the indicated temperature. CT26 cells were incubated with Fe-NBM for 2 h and then heated in different temperature for 5 min. (d) Western blot image of CETSA of IRE1α after CT26 cells treated by different concentrations of Fe-NBM under 58 °C. (e, f) Western blot image of XBP1s and ATF6.

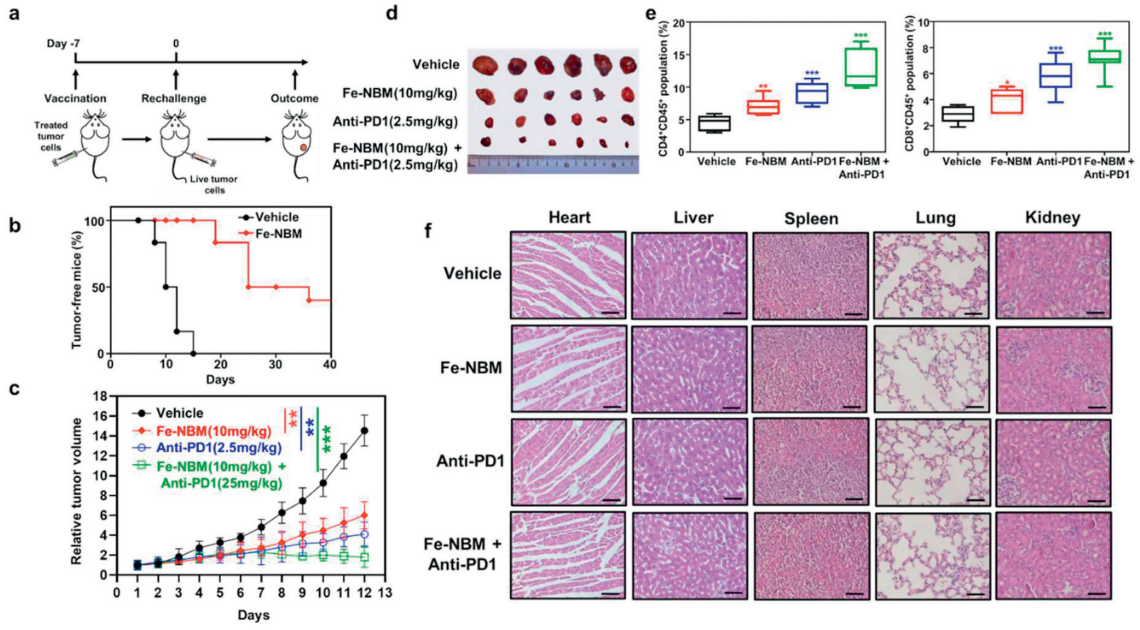


Fig. 6. Fe-NBM induces ICD *in vivo* and enhances anti-PD1 immunotherapy. (a) Schematic illustration of the timeline for immunocompetent mouse model. (b) Tumour-free mice curve of vaccination model. (c) The tumour volume over the treatment period. The treatment methods were as follows: The abscopal antitumor activity was evaluated in CT26 tumour bearing mice models developed by injecting CT26 cells into both the right and left flank regions of BALB/c mice while the right tumours were designated the primary tumours for the treatment of Fe-NBM and the left tumours were designated the distant tumours and did not receive Fe-NBM treatment. The mice were divided into four groups (Group 1: vehicle, PBS only; Group 2: Fe-NBM (10 mg/kg) only; Group 3: anti-PD1 (2.5 mg/kg) only; Group 4: Fe-NBM+anti-PD1). (d) Photographs of the collected tumours after the tumour volumes reached 1500 mm^3. (e) The CD4/CD8 activations after different treatment were detected by flow cytometer. (f) H&E staining of major organs after different treatments, scale bars: 100 μm. Mean ± SD. $^*P < 0.05$; $^{**}P < 0.01$; $^{***}P < 0.001$.

nificant tumor growth was observed in the Fe-NBM-treated group (Fig. 6b), which indicated that CT26 cells treated with Fe-NBM would undergo ICD and act as vaccines to stimulate anti-tumor immunity.

Studies found that ICD could improve T cell responses, which means ICD may further evoke anti-tumor immunity elicited by anti-PD1 [59]. We examined whether Fe-NBM could enhance the anti-tumor immunity of anti-PD1 by CT26 subcutaneous tumor model. All mice were randomly divided into four groups (Group 1: vehicle, PBS only; Group 2: Fe-NBM only; Group 3: anti-PD1 only; Group 4: Fe-NBM + anti-PD1). Tumor volume was monitored for 13 days. Compared with the Fe-NBM or anti-PD1 monotherapy groups, Fe-NBM + anti-PD1 group led to a significantly enhanced anti-tumor effect and almost fully blocked the tumor growth of CT26 cells (Figs. 6c and d). To validate the activation of immune response *in vivo*, we evaluated the T cell infiltration in the distant tumor tissues by flow cytometry. As shown in Fig. 6e, the number of infiltrating $CD4^+$ and $CD8^+$ T cells was remarkably increased in Fe-NBM + anti-PD1 group, which suggested that compared with Fe-NBM or anti-PD1 monotherapy groups, Fe-NBM + anti-PD1 group had an enhanced T-cell-related anti-tumor immune response (Fig. S24 in Supporting information). Meanwhile, the body weight of these four groups showed no significant difference (Fig. S25 in Supporting information). The histological examination (H&E) staining of the main organs (heart, liver, spleen, lungs, kidneys) demonstrated no significant histological damage (Fig. 6f). All these results indicated that Fe-NBM could enhance expansion of $CD4^+$ and $CD8^+$ T cells, thus generated robust anti-tumor immunity and enhanced the anti-tumor therapeutic efficacy of anti-PD1 with no significant toxic side effect.

In summary, a well configured iron(II) complex (Fe-NBM) was obtained through the solvothermal domino reaction of readily available substrates in one pot. Besides, the reaction mechanism was thoroughly studied by capturing a series of intermediates with ESI-MS and crystallography. This step-economy domino reaction differs from the conventional stepwise methodology for the construction of metal complexes, which involves the initial synthesis of ligands and subsequent coordination with metal ions. Hence, this approach also provides a platform for rapid access to potential metal-based ICD inducers.

Next, we have demonstrated that Fe-NBM, due to its redox properties, could facilitate the generation of $^{\bullet}OH$ from H_2O_2 in both extracellular and intracellular environments. Cellular experiments revealed that Fe-NBM was able to inhibit the growth of cancer cells, and trigger the release of ICD-related DAMPs within CT26 cells. The results of RNA-seq further identified the increase in the expression of immune-related genes promoted by Fe-NBM. Specially, CLSM and CETSA experiments indicated that Fe-NBM could targeted the ER selectively by binding to IRE1α. *In vivo* experiments elucidated that Fe-NBM could activate the anti-tumor immune response system, significantly enhancing anti-PD1 immunotherapy. Additionally, H&E staining indicated that Fe-NBM showed no significant toxicity on major organs. In this study, we develop the first iron(II) complex, Fe-NBM, which works as an effective ICD inducer through binding to IRE1α, targeting the ER, provoking UPR and generating ROS. Our research inspires the step-economy strategy of novel ICD inducers' fabrication with special target effect.

Declaration of competing interest

The authors declare that they have no known competing financial interests or personal relationships that could have appeared to influence the work reported in this paper.

CRediT authorship contribution statement

Ning Tian: Writing – original draft, Data curation. **Haoyu Ju:** Writing – original draft, Data curation. **Qian Hu:** Methodology, Data curation. **Qifeng Hou:** Methodology. **Yiping Lu:** Methodology. **Yu Liu:** Methodology. **Jinmei Huang:** Methodology. **Zhong-Hong Zhu:** Methodology. **Bin Zhang:** Writing – review & editing. **Jin Huang:** Writing – review & editing, Conceptualization. **Ming-Hua Zeng:** Writing – review & editing, Conceptualization.

Acknowledgments

This work was supported by the BAGUI Talent Program of Guangxi Province (No. 2019AC26001), the National Natural Science Foundation of China (Nos. U23A2080, 82373913, 22171075), and the Shanghai Frontiers Science Center of Optogenetic Techniques for Cell Metabolism (No. SKLDR-2023-KF-04).

Supplementary materials

Supplementary material associated with this article can be found, in the online version, at doi:10.1016/j.cclet.2025.111038.

References

[1] G. Kroemer, L. Zitvogel, O. Kepp, et al., Annu. Rev. Immunol. 31 (2013) 51–72.
[2] A.D. Garg, A.M. Dudek-Peric, E. Romano, et al., Int. J. Dev. Biol. 59 (2015) 131–140.
[3] D.V. Krysko, A.D. Garg, A. Kaczmarek, et al., Nat. Rev. Cancer 12 (2012) 860–875.
[4] A.P. King, J.J. Wilson, Chem. Soc. Rev. 49 (2020) 8113–8136.
[5] S. Sen, M. Won, M.S. Levine, et al., Chem. Soc. Rev. 51 (2022) 1212–1233.
[6] L. Zhang, N. Montesdeoca, J. Karges, et al., Angew. Chem. Int. Ed. 62 (2023) e202300662.
[7] S. Sen, K. Karoscik, E. Maier, et al., Curr. Opin. Chem. Biol. 73 (2023) 102277.
[8] J. Karges, R.W. Stokes, S.M. Cohen, Trends. Chem. 3 (2021) 523–534.
[9] M. Lv, Y. Zheng, J. Wu, et al., Angew. Chem. Int. Ed. 62 (2023) e202312897.
[10] L.Y. Liu, T.Z. Ma, Y.L. Zeng, et al., Angew. Chem. Int. Ed. 62 (2023) e202305645.
[11] D.Y.Q. Wong, W.W.F. Ong, W.H. Ang, Angew. Chem. Int. Ed. 54 (2015) 6483–6487.
[12] M.J.R. Tham, M.V. Babak, W.H. Ang, Angew. Chem. Int. Ed. 59 (2020) 19070–19078.
[13] Z. Deng, N. Wang, Y. Liu, et al., J. Am. Chem. Soc. 142 (2020) 7803–7812.
[14] L. Wang, R. Guan, L. Xie, et al., Angew. Chem. Int. Ed. 60 (2021) 4657–4665.
[15] C. Li, L. Tu, Y. Xu, et al., Angew. Chem. Int. Ed. 62 (2024) e202406392.
[16] L. Wang, R. Guan, L. Xie, et al., Angew. Chem. Int. Ed. 60 (2021) 4657–4665.
[17] X. Xiong, K.B. Huang, Y. Wang, et al., J. Am. Chem. Soc. 144 (2022) 10407–10416.
[18] W. Lin, Y. Liu, J. Wang, et al., Angew. Chem. Int. Ed. 62 (2023) e202310158.
[19] M. Lv, Y. Zhang, J. Wu, et al., Angew. Chem. Int. Ed. 62 (2023) e202312897.
[20] L. Wang, J. Karges, F. Wei, et al., Chem. Sci. 14 (2023) 1461–1471.
[21] T. Feng, Z. Tang, J. Karges, et al., Chem. Sci. 15 (2024) 6752–6762.
[22] Z. Zhao, X. Wang, J. Wang, et al., J. Med. Chem. 66 (2023) 11951–11964.
[23] L. Tu, C. Li, Q. Ding, et al., J. Am. Chem. Soc. 146 (2024) 8991–9003.
[24] Y. Lu, D. Zhu, Y. Wang, Small 20 (2024) 2310636.
[25] S. Sen, S. Hufnagel, E.Y. Maier, et al., J. Am. Chem. Soc. 142 (2020) 20536–20541.
[26] R.D. Mule, A. Kumar, S.P. Sancheti, et al., Chem. Sci. 13 (2022) 10779–10785.
[27] Z. Xu, Q. Lu, M. Shan, et al., J. Med. Chem. 66 (2023) 7813–7833.
[28] F. Li, Z. Wen, C. Wu, et al., J. Med. Chem. 67 (2024) 1982–2003.
[29] K.B. Huang, F.Y. Wang, Y. Lu, et al., PANS 121 (2024) e2404668121.
[30] J.N. Smith, P. Kaur, K. Suntharalingam, Eur. J. Inorg. Chem. 2021 (2021) 1770–1775.
[31] P. Kaur, A. Johnson, J. Northcote-Smith, et al., ChemBioChem 21 (2020) 3618–3624.
[32] K.D. Mjos, C. Orvig, Chem. Rev. 114 (2014) 4540–4563.
[33] J.P. Zhong, B. Liu, Y. Tao, et al., Inorg. Chem. 56 (2017) 10123–10126.
[34] B. Liu, F. Yu, M. Tu, et al., Angew. Chem. Int. Ed. 58 (2019) 3748–3753.
[35] M.H. Zeng, Z. Yin, Z.H. Liu, et al., Angew. Chem. Int. Ed. 55 (2016) 11407–11411.
[36] Z.H. Zhu, Q. Hu, H.L. Pan, et al., Sci. China Chem. 62 (2019) 719–726.
[37] M. Zeng, Y. Xue, Y. Qin, et al., Chin. Chem. Lett. 33 (2022) 4891–4895.
[38] C. Hetz, K. Zhang, R.J. Kaufman, Nat. Rev. Mol. Cell Biol. 21 (2020) 421–438.
[39] M. Ciaccia, S.D. Stefano, Org. Biomol. Chem. 13 (2015) 646–654.
[40] H. Cheng, Y. Yang, Y. Wang, et al., Adv. Funct. Mater. 34 (2024) 2405421.
[41] X. Li, Q. Zhou, D. Dutta, et al., ACS Nano 16 (2022) 14982–14999.
[42] C. Gorrini, I.S. Harris, T.W. Mak, Nat. Rev. Drug Discov. 12 (2013) 931–947.
[43] X. Chen, C. Shi, M. He, et al., Signal. Transduct. Target. Ther. 8 (2023) 352.
[44] R.V. Rao, H. Ellerby, D.E. Bredesen, Cell Death. Differ. 11 (2004) 372–380.
[45] M. Cnop, S. Toivonen, M. Igoillo-Esteve, et al., Mol. Metab. 6 (2017) 1024–1039.
[46] J. He, Y. Zhou, L. Sun, Cell Commun. Signal. 22 (2024) 89.
[47] E. Vénéreau, C. Ceriotti, M.E. Bianchi, Front. Immune 6 (2015) 422.
[48] L. Galluzzi, E. Guilbaud, D. Schmidt, et al., Nat. Rev. Drug Discov. 23 (2024) 445–460.
[49] L. Galluzzi, A. Buqué, O. Kepp, et al., Nat. Rev. Immunol. 17 (2017) 97–111.
[50] I. Martins, Y. Wang, M. Michaud, et al., Cell Death. Differ. 21 (2014) 79–91.
[51] G.P. Sims, D.C. Rowe, S.T. Rietdijk, et al., Annu. Rev. Immunol. 28 (2010) 367–388.
[52] J. Fucikova, O. Kepp, L. Kasikova, et al., Cell Death. Dis. 11 (2020) 1013.
[53] G. Volpi, R. Rabezzana, New. J. Chem. 45 (2021) 5737–5743.
[54] O. Trott, A.J Olson, J. Comput. Chem. 31 (2010) 455–461.
[55] D.M. Molina, R. Jafari, M. Ignatushchenko, et al., Science 341 (2013) 84–87.
[56] Y. Lu, F.X. Liang, X. Wang, Mol. Cell 55 (2014) 758–770.
[57] T. Yan, X. Ma, L. Guo, et al., Cancer Biol. Med. (2023), doi:10.20892/j.issn.2095-3941.2023.0232.
[58] P. Tsaytler, H.P. Harding, D. Ron, et al., Science (1979) 332 (2011) 91–94.
[59] Y. Li, H. Zhang, Q. Li, et al., Cancer Lett. 495 (2020) 12–21.